16th Australasian Fluid Mechanics Conference
Crown Plaza, Gold Coast, Australia
2-7 December 2007

Surface Acoustic Wave Driven Microchannel Flow

M. K. Tan, J. R. Friend and L. Y. Yeo[1]

[1]Micro/Nanophysics Research Laboratory
Monash University, Clayton, Victoria 3800, Australia

Abstract

We demonstrate that the propagation of surface acoustic waves, arising from the excitation of the acoustic field on a piezoelectric crystal (lithium niobate) substrate, along the sidewalls of microchannels (50 μm or 280 μm wide and 200 μm deep) fabricated in the substrate, can give rise to throughflow with velocities of the order 10 mm/s. This streaming flow in the direction along which the surface acoustic wave propagates is a result of the leakage of acoustic radiation from the substrate walls into the fluid. Good agreement is obtained between these preliminary experimental results with those from numerical simulations of the classical acoustic streaming model. In any case, these results show the potential of surface acoustic wave micropumps to be an effective fluid-driving mechanism for microfluidic devices.

Introduction

Surface acoustic waves (SAWs) are generated by applying a high-frequency signal to an interdigital transducer (IDT) fabricated on a lithium niobate ($LiNbO_3$, LN) substrate. When coupled with a water droplet, the wave is diffracted into the droplet at the Rayleigh angle and thus imparts an acoustic streaming force on the fluid [1, 2]. Depending on the power level of the excitation, a range of responses from the droplet may be observed. As the power is progressively increased, drop vibration and subsequently translation along the SAW propagation direction [3, 4, 5] gives way to streaming jets [6] and finally atomization [7].

Tseng *et al.* [8] have experimentally demonstrated a SAW driven micromixer using a 9.6 MHz SAW device. The width and height of their microchannel were 200 μm and 100 μm, respectively. This U-shape PDMS microchannel was then bonded directly on top of the LN substrate that formed the single radiator configuration. For micromixing, the induced streaming vortex in the microchannel is more important than uniform fluid flow along the channel. Sritharan *et al.* [9], on the other hand, exploited a hybrid system for SAW induced microchannel mixing by placing a 146 MHz SAW device directly underneath a substrate which has a microchannel with dimensions 100 μm in height and 75 μm in width fabricated onto it. The SAW device was oriented such that the surface waves propagate in the direction transverse to the flow to induce vortices in the channel. In this paper, we propose a new configuration using a 20 MHz SAW device that enables the generation of microchannel flow for micropumping applications. Unlike the previous micromixing studies, we wish to avoid the generation of vortices that disrupt the throughflow; in fact, we show that this is true when the aspect ratio of the microchannel is large. In addition, we also present a numerical analysis that allows a simplified prediction of the flow field.

To the best of our knowledge, only two microdevices that employ acoustic streaming for micropumping have been previously reported; the flexural plate wave (FPW) actuation mechanism [10] and the direct coupling of a PZT transducer to a microchannel for upstream streaming actuation [11]. While sufficient flow velocity (~ 150 μm/s) is attainable using the FPW actuation, the device fabrication is rather complex. Similarly, the direct coupling of the PZT transducer to a microchannel is able to generate 1 mm/s order flow velocities but suffers from the low pressure head (< 1 Pa) in high-impedance systems. The velocities generated using SAW reported here is typically around 10 mm/s. Moreover, the SAW device we propose is relatively easy to fabricate.

Experiments

The substrate used was a 500 μm thick 128° rotated Y-cut X-propagating LN substrate. A pair of bidirectional interdigital transducers were fabricated on the substrate to excite the surface wave at 20 MHz frequency. The laser ablated groove type microchannel has a rectangular cross section, as shown in Fig. 1(a) and has dimensions 200 μm deep and 10 mm long; two channel widths, 50 μm and 280 μm, were used. A damping material (α-gel, Geltec Ltd., Yokohama, Japan) was attached to the substrate edges to prevent wave reflection. Measurements of the displacement perpendicular to the substrate surface using a scanning laser doppler vibrometer (MSA400, Polytec PI, Waldbrunn, Germany) shows that the vibration amplitudes were higher along the edges between the ablated regions and the substrate surface in an open channel configuration, i.e. no coverslip present. Fluorescent microspheres (BioScientific, Gymea NSW) of diameter 1 μm were employed to aid visualisation of the flow field. The particle motion was recorded using a high speed video camera (MotionBLITZ HSC-kit, Mikrotron, Germany) at a rate of 500 frames/second connected to a microscope (50X magnification) focused on planes at different depth in the microchannel (Fig. 1(b)).

Figures 1(c) and 1(d) show the SAW actuated fluid motion in 50 μm and 280 μm wide microchannels, respectively. The flow velocities in the 50 μm groove type channel, approximately 3.5 mm/s, appear to be predominantly unidirectional across the channel width, whereas vortices were observed to form when the microchannel width was increased to 280 μm; the flow velocity in the case of this larger channel width, nevertheless, is much larger, typically about 55 mm/s. The appearances of vortices in larger channels is consistent with our numerical predictions which we will present in the next section. Along Plane C–C close to the bottom of the channel, as depicted in Fig. 1(b), particles were observed to assemble along nodal lines despite a net albeit weaker throughflow (Fig. 1(e)); typical velocities at this channel depth are less than 1 mm/s. This suggests that at the bottom of the channel, streaming velocities are relatively weak and the waves radiated from the two acoustic waves that travel along the sidewalls superimpose to form a standing acoustic wave within the channel.

Particle concentration along the nodal lines in a standing sound field has been demonstrated by Sobanski *et al.* [12] experimentally. Here, we briefly consider a comparison between the Rayleigh-type acoustic streaming force and the particle drift force of Vainshtein *et al.* [13]. The characteristic streaming velocity is approximately $u_s = 3\xi_0^2/8c \sim 10^{-7}$ m/s, where ξ_0 is the amplitude of the fluid particle oscillation and c is the speed

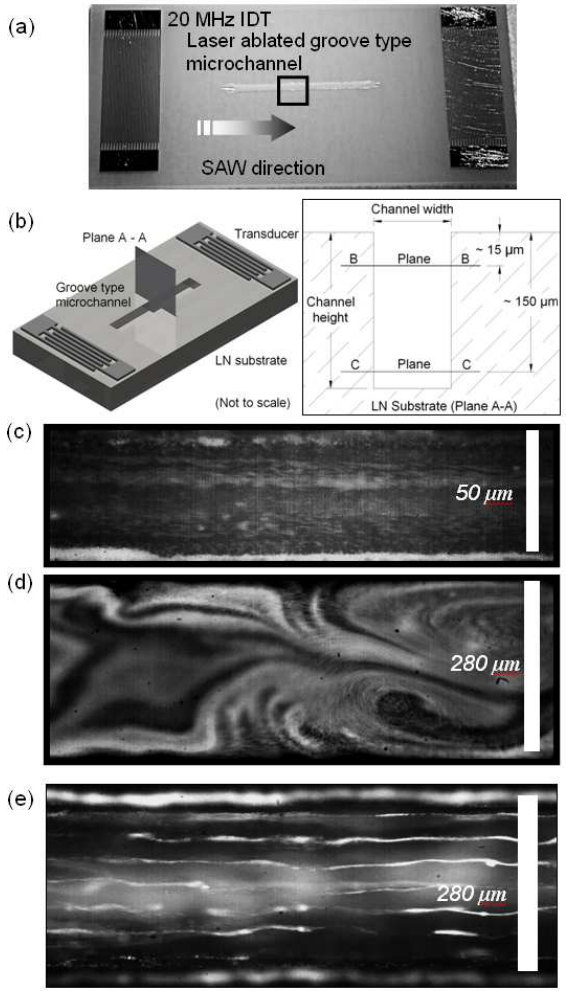

Figure 1: (a) Laser ablated microchannel on a 20 MHz SAW device. (b) Schematic illustration defining the different viewing planes on which the microscope lens is focused. (c) Particle streaklines along Plane B–B in a 50 μm wide channel and (d) in a 280 μm wide channel, and, (e) along Plane C–C in a 280 μm wide channel.

of sound in water; our estimation for the acoustic velocity of the fluid particles adjacent to the surface u_0 was based on our numerical results, which we will discuss subsequently. On the other hand, the particle drift velocity is approximately $u_D = 3\omega\tau u_0^2/4c \sim 10^{-6}$ m/s for 1 μm polystyrene particles suspended in water, where ω is the angular frequency and $\tau = \rho_p d^2/18\mu$ is the Stokes particle relaxation time; ρ_p, d and μ denotes the particle density, particle diameter and fluid viscosity, respectively. Given that the characteristic streaming velocity is approximately one order in magnitude smaller than the particle drift velocity, it then becomes obvious that point aggregation of the particles should occur under these conditions. However, due to the slenderness of the channel, particles rather non-uniformly concentrate along the nodal lines than on the nodal points. At Plane B–B close to the top of the channel (Fig. 1(b)), particle aggregation along nodal lines is not observed since the streaming force is sufficiently strong such that it convects the particles along with the moving fluid (Figs. 1(c) and (d)).

Numerical analysis

A rectangular Cartesian coordinate system x_i (i=1,2,3) is employed, with x_1 defined along the SAW propagation direction,

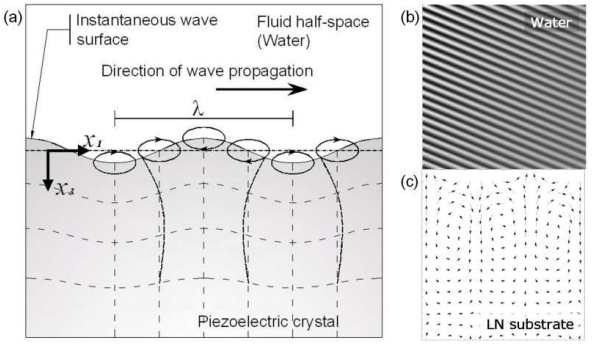

Figure 2: SAW propagation on a semi-infinite LN substrate coupled with water. (a) Motion of the solid particle elements of the LN substrate. (b) The radiated acoustic wave in water at the Rayleigh angle. (c) Vector plot of the particle displacement in the solid. Note that the particle displacement amplitude decays exponentially into the LN substrate.

and x_3 defined to be perpendicular to the substrate plane and positive into the solid. The system may be modelled in the coupled fluid-solid half-space domain, Fig. 2(a), with the solid half-space defined by $x_3 > 0$, and the fluid by $x_3 < 0$. The partial differential equations governing the displacement and electric field potential in the piezoelectric crystal medium are [14, 15]:

$$C_{ijkl}\xi_{k,li} + e_{kij}\varphi_{,ki} = \rho_s\ddot{\xi}_j, \tag{1}$$

and

$$e_{ikl}\xi_{k,li} - \varepsilon_{ik}\varphi_{,ki} = 0, \tag{2}$$

where ρ_s, φ, C_{ijkl}, e_{kij}, and ε_{ik} is the crystal mass density, electric potential, elastic stiffness constant, piezoelectric constant, and dielectric constant, respectively. An index preceded by a comma denotes differentiation with respect to the spatial coordinates, whereas the dot notation is employed to imply differentiation with respect to time. In the crystal medium ($x_3 > 0$), the traveling wave has the solutions of the form [15]:

$$\xi_i = \beta_i \exp[-\alpha_s\omega x_3/v_s]\exp[j\omega(t - x_1/v_s)], \tag{3}$$

and

$$\varphi = \beta_4 \exp[-\alpha_s\omega x_3/v_s]\exp[j\omega(t - x_1/v_s)], \tag{4}$$

where v_s is the surface wave velocity.

The solutions are then substituted into the differential equations given by Eqs. (1) and (2), giving rise to a linear homogeneous system of four equations. For the nontrival solution to exist, the determinant of the coefficients must be zero. Upon obtaining the four appropriate values of α_s, the corresponding values of β_i can be found from each value of α_s. The coupled field in the crystal is expressed as the linear combination of the partial fields:

$$\xi_i = \sum_{l=1}^{4} B^{(l)}\beta_i^{(l)} \exp[-\alpha_s^{(l)}\omega x_3/v_s]\exp[j\omega(t - x_1/v_s)], \tag{5}$$

$$\varphi = \sum_{l=1}^{4} B^{(l)}\beta_4^{(l)} \exp[-\alpha_s^{(l)}\omega x_3/v_s]\exp[j\omega(t - x_1/v_s)]; \tag{6}$$

the amplitude coefficients $B^{(1)}$, $B^{(2)}$, $B^{(3)}$, and $B^{(4)}$ are determined by the solid-liquid boundary conditions [15].

The behaviour of the fluid in the domain $x_3 < 0$, on the other hand, obeys the following equations governing mass and momentum conservation:

$$\frac{\partial\rho_f}{\partial t} + \nabla\cdot(\rho\mathbf{u}) = 0, \tag{7}$$

and

$$\rho_f \frac{\partial \mathbf{u}}{\partial t} + \rho_f (\mathbf{u}\cdot\nabla\mathbf{u}) = -\nabla p + \mu\nabla^2\mathbf{u} + \left(\eta + \frac{4\mu}{3}\right)\nabla\nabla\cdot\mathbf{u}, \quad (8)$$

in which ρ_f, η, μ is the fluid density, bulk viscosity, and shear viscosity, respectively. Assuming a small parameter $\varepsilon = u_0/c \ll 1$, we assume a regular perturbation expansion in the asymptotically small ε limit:

$$(p - p_0, \rho - \rho_0, \mathbf{u}) = (p_1, \rho_1, \mathbf{u}_1) + \varepsilon((p_2, \rho_2, \mathbf{u}_2) + \ldots \quad (9)$$

$\mathbf{u}_1$ is therefore the leading order acoustic velocity and $\mathbf{u}_2$ is the streaming velocity. We note that the higher order correction terms involve both the steady and harmonic fields. Nevertheless, we seek only the steady terms since we are interested in the streaming velocity $\mathbf{u}_2$ [16, 17].

Following [16, 17, 18], we decompose the leading order velocity $\mathbf{u}_1$ into the sum of contributions from an irrotational longitudinal $\mathbf{u}_l$, i.e. $\nabla\times\mathbf{u}_l = 0$, and an incompressible tranverse component $\mathbf{u}_t$ that satisfies $\nabla\cdot\mathbf{u}_t = 0$. The leading order approximation to Eq. (8) can then be written as

$$\rho_f \frac{\partial \mathbf{u}_l}{\partial t} = \left(\eta + \frac{4\mu}{3}\right)\nabla^2\mathbf{u}_l, \quad (10)$$

and

$$\rho_f \frac{\partial \mathbf{u}_t}{\partial t} = -\mu\nabla\times\nabla\times\mathbf{u}_t. \quad (11)$$

In Eq. (10), we have omitted the leading order pressure gradient ∇p_1 following [15], assuming that the compressional wave contribution to the leading order field as well as the frequency dependent pressure relaxation contribution is negligible. In addition to the above, we also require the electric potential field in fluid medium, which obeys $\nabla^2\varphi = 0$ [15].

Given the decoupling between the velocity and electric potential in the above, we then admit the following solutions for the particle displacement (time integral of the leading order velocity field) and potential in the fluid phase[15]:

$$\xi_i^{(l)} = \gamma_i \exp[-\alpha_f \omega x_3/v_s]\exp[j\omega(t - x_1/v_s)], \quad (12)$$

and

$$\varphi^{(l)} = C\exp[-\alpha_f \omega x_3/v_s]\exp[j\omega(t - x_1/v_s)]. \quad (13)$$

By substituting Eq. (12) into Eq. (10), we obtain

$$\alpha_f = \sqrt{\frac{(\eta + \mu\omega/3) - v_s^2\rho_f}{(\eta + \mu\omega/3)}}, \quad (14)$$

and

$$\gamma_1 = \frac{j(\eta + \mu\omega/3)\alpha_f}{(\eta + \mu\omega/3) - \rho_f v_s^2}\gamma_3. \quad (15)$$

A possible solution to Eq. (11) would then consist of a transverse shear viscous wave which satisfies $\nabla\cdot\mathbf{u}_t = 0$ has a velocity of the form [18]:

$$u_t = A\exp\left[j\omega t - \frac{(j-1)}{d_v}x_3\right], \quad (16)$$

in which $d_v = \sqrt{(2\mu)/(\rho_f\omega)} \approx 10^{-6}$ m is the viscous boundary layer thickness. We note that only the transverse solution is important near the boundary. The amplitude coefficient A in Eq. (16) is determined by the no-slip boundary condition at the fluid-solid interface.

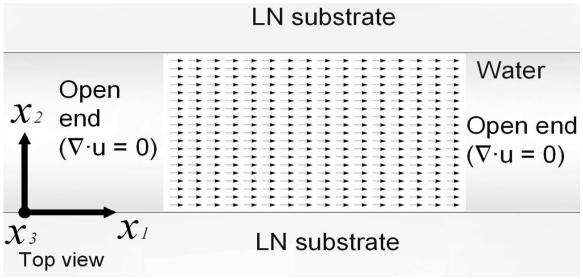

Figure 3: Schematic of the microchannel flow driven by SAW along the side walls as viewed from above. The calculated velocity vector from the numerical model is shown for a 50 μm width channel.

The boundary conditions employed to find the amplitude coefficients for the coupled field are continuity of fluid velocity at the interface between the boundary layer and the bulk fluid medium, continuity of electric potential, continuity of the normal component of electric displacement and continuity of normal stresses at the fluid-solid interface. Substituting the coupled field Eqs. (5), (6), (12), (13), and (16) into the boundary conditions, we obtain six homogeneous equations with the six unknown amplitude coefficients $B^{(1)}$, $B^{(2)}$, $B^{(3)}$, $B^{(4)}$, C, and γ_3. In order to obtain v_s, the determinant of the matrix coefficient must be zero for the nontrivial solution to exist.

The next order correction to Eq. (8) is [16]:

$$\mathbf{F}_2 = -\frac{1}{c^2}\langle p_1\frac{\partial \mathbf{u}_1}{\partial t}\rangle - \rho_f\langle(\mathbf{u}_1\cdot\nabla)\mathbf{u}_1\rangle, \quad (17)$$

where the body force density $\mathbf{F}_2$ is given by

$$\mathbf{F}_2 = \nabla p_2 - \mu\nabla^2\mathbf{u}_2 - \left(\eta + \frac{\mu}{3}\right)\nabla\nabla\cdot\mathbf{u}_2, \quad (18)$$

The parenthesis $\langle\cdot\rangle$ denotes time-averaging of the inner quantities. The leading order velocity field $\mathbf{u}_1$, obtained from the coupled field with piezoelectric crystal, is then substituted into Eq. (17) to obtain the body force distribution, from which Eq. (18) can then solved for the streaming velocity, $\mathbf{u}_2$. Together with the continuity equation describing the conservation of mass of an incompressible fluid, $\nabla\cdot\mathbf{u}_2 = 0$, we then proceed to rearrange Eqs. (17) and (18) such that Eq. (18) is reduced to an elliptic partial differential equation, which we can solve numerically using a finite-volume method. To account for the pressure correction in Eq. (18), the SIMPLER algorithm for a staggered mesh is used [19].

Figure 3 shows the proposed microchannel configuration commensurate with that employed in the experiments. Numerical results are presented in Fig. 4; these results are based on the assumption that no waves are reflected from the walls and that the waves on both walls have equal amplitude. The predicted flow velocities for the 50 μm channel ($\sim$ 6 mm/s) the 280 μm channel ($\sim$ 50 mm/s) are close to the experimental results ($\sim$ 3.5 mm/s for the 50 μm channel and $\sim$ 55 mm/s for the 280 μm channel). The calculated pressures p_2 for the 50 μm and 280 μm channels are typically 5–20 Pa and 200–400 Pa, respectively. We observe from Fig. 4(b) that the the transverse velocities (along the x_2 direction) are no longer insignificant, and could give rise to the onset of the flow vortices observed in the experiments (Fig. 1(d)). In any case, the results indicate that the net throughflow along the x_1-direction (in the direction parallel to the walls) for effective micropumping applications is possible provided that the channel aspect ratio is sufficiently large such that the transverse velocities are insignificant (Fig. 4(a)).

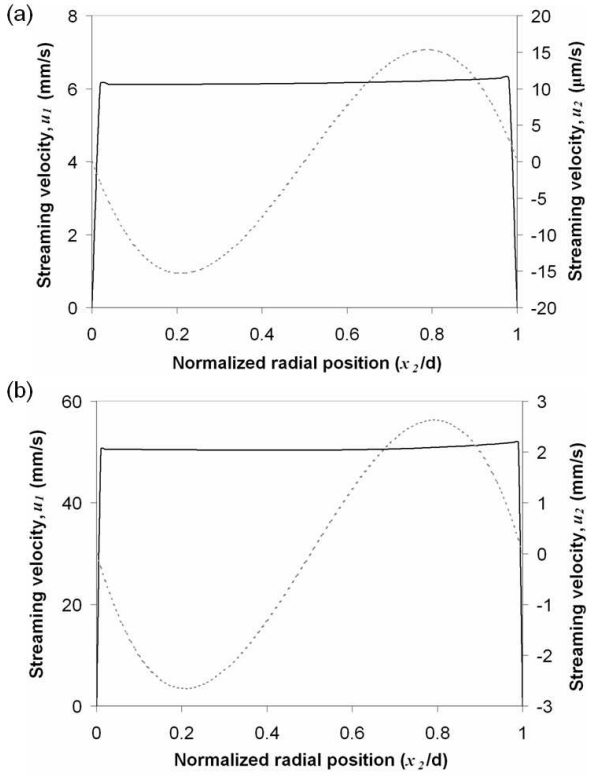

Figure 4: Streaming velocities driven by a travelling SAW for both (a) 50 μm and (b) 280 μm channel widths. The solid dark lines are the x_1-components of the velocity, and, the dashed grey lines are the x_2-components of the streaming velocity. The predicted flow velocities are consistent with the experimental results for both channel widths.

Conclusions

A promising scheme using surface acoustic waves to pump fluids in microchannels is demonstrated. Flow velocities of up to 10 mm/s in a 50 μm wide microchannel and in excess of this for larger microchannels were observed with a 20 MHz SAW device. The flow is unidirectional along the direction of the SAW propagation for smaller channels where the width is less than the SAW wavelength. When the channel width becomes commensurate with the SAW wavelength, the flow, although having larger velocities, becomes increasingly chaotic with the appearance of vortices within the channel. Although this is perhaps unsuitable for micropumping, these flows could have important consequences for channel micromixing. Close to the bottom of the channel where the acoustic streaming is weak due to the no-slip condition at the channel floor, the particles are observed to drift and hence aggregate along nodal lines. Good agreement is obtained between the numerical predictions and experimental observations of the flow field.

References

[1] T. Uchida, T. Suzuki and S. Shiokawa, Investigation of acoustic streaming excited by surface acoustic waves, *1995 IEEE Ultrasonics Symposium*, 1995, vol. 2, pp. 1081–1084.

[2] H. Li, J. R. Friend and L. Y. Yeo, Surface acoustic Wave concentration of particle and bioparticle suspensions. *Biomed. Microdev.*, 2007, **9**, 2007, 647–656.

[3] A. Wixforth, Acoustically driven planar microfluidics, *Superlatt Microstruct.*, **33**, 2003, 389–396.

[4] M. K. Tan, J. R. Friend and L. Y. Yeo, Microparticle collection and concentration via a miniature surface acoustic wave device, *Lab Chip*, **7**, 2007, 618–625.

[5] A. Renaudin, P. Tabourier, V. Zhang, J. C. Camart and C. Druon, SAW nanopump for handling droplets in view of biological applications, *Sens. Act. B*, **113**, 2006, 389–397.

[6] Sir J. Lighthill, Acoustic streaming, *J. Sound Vib.*, **61**, 1978, 391–418.

[7] K. Chono, N. Shimizu, Y. Matsui, J. Kondoh and S. Shiokawa, Development of noval atomization system based on SAW streaming, *Jap. J. Appl. Phys.*, **43**, 2004, 2987–2991.

[8] W. K. Tseng, J. L. Lin, W. C. Sung, S. H. Chen, and G. B. Lee, Active micro-mixers using surface acoustic waves on Y-cut 128° $LiNbO_3$, *J. Micromech. Microeng.*, **16**, 2006, 539–548.

[9] K. Sritharan, C. J. Strobl, M. F. Schneider, A. Wixforth, and Z. Guttenberg, Acoustic mixing at low Reynolds numbers, *Appl. Phys. Lett.*, **88**, 2006, 054102.

[10] C. E. Bradley, J. M. Bustillo and R. M. White, Flow measurement in a micromachined flow system with integrated acoustic pumping, *1995 IEEE Ultrasonics Symposium*, 1995, vol. 1, pp. 505–510.

[11] J. C. Rife, M. I. Bell, J. S. Horwitz, M. N. Kabler, R. C. Y. Auyeung and W. J. Kim, Miniature valveless ultrasonic pumps and mixers, *Sens. Act. A*, **86**, 2000, 135–140.

[12] M. A. Sobanski, C. R. Tucker, N. E. Thomas and W. T. Coakley, Sub-micron particle manipulation in an ultrasound standing wave: Applications in detection of clinically important biomolecules, *Bioseparation*, **9**, 2001, 351–357.

[13] P. Vainshtein, M. Fichman, K. Shuster, and C. Gutfinger, The effect of centreline particle concentration in a wave tube, *J. Fluid Mech.*, **306**, 1996, 31–42.

[14] H. F. Tiersen, Wave propagation in an infinite piezoelectric plate, *J. Acoust. Soc. Am.*, **35**, 1963, 234-239.

[15] J. J. Campbell and W. R. Jones, A method for estimating optimal crystal cuts and propagation directions for excitation of piezoelectric surface waves, *IEEE Trans. Sonics and Ultrasonics*, **15**, 1968, 209-217.

[16] W. L. Nyborg, *Acoustic streaming*, San Diego, Academic, 1965, 265-331.

[17] C. E. Bradley, Acoustic streaming field structure: the influence of the radiator, *J. Acoust. Soc. Am.*, **100**, 1996, 1399–1408.

[18] P. M. Morse and K. U. Ingard, *Theoretical acoustics*, McGraw-Hill, 1968.

[19] S. V. Patankar, *Numerical heat transfer and fluid flow*, Hemisphere, 1980, p. 131.